Acta Materialia 264 (2024) 119574

Contents lists available at ScienceDirect

Acta Materialia

journal homepage: www.elsevier.com/locate/actamat

Full length article

Differences in structure and dynamics of ternary Pd–Ni-based bulk metallic glasses containing sulfur or phosphorous

Hendrik Voigt [a,*], Nico Neuber [b], Olivia Vaerst [a], Maximilian Demming [a], Ralf Busch [b], Martin Peterlechner [c], Harald Rösner [a], Gerhard Wilde [a]

[a] University of Münster, Institute of Materials Physics, Wilhelm-Klemm-Str. 10, Münster, 48149, Germany
[b] Saarland University, Chair of Metallic Materials, Campus C6.3, Saarbrücken, 66123, Germany
[c] Laboratorium für Elektronenmikroskopie, Karlsruhe Institute of Technology, Engesserstraße 7, Karlsruhe, 76131, Germany

ARTICLE INFO

Keywords:
Sulfur bearing bulk metallic glass
Fluctuation electron microscopy
Diffraction
Electron correlation microscopy
Glassy dynamics
Medium-range order

ABSTRACT

The composition $Pd_{31}Ni_{42}S_{27}$ has been shown to be the best glass former in the family of recently discovered glass forming PdNiS alloys. In this study, this sample system was systematically investigated using fluctuation- and correlation electron microscopy of which the results are compared to a $Pd_{40}Ni_{40}P_{20}$ bulk metallic glass that serves as a model system for metallic glasses. Strong differences in the local atomic correlations beyond the short-range order were observed, which are assumed to be a reason for their discrepancy in thermal stability. The relaxation dynamics at room temperature revealed faster dynamics in the sulfur-containing $Pd_{31}Ni_{42}S_{27}$ glass.

1. Introduction

Metallic glasses have been the subject of intensive research since their discovery in the 1960s [1,2]. Since then, new alloy classes that form bulk metallic glasses (BMG) upon melt quenching have been reported, with sulfur-containing alloys being a very recent addition [3,4]. Within this new alloy class that allows bulk glass formation, PdNiS-alloys show the highest glass forming ability (GFA). Compositionally, these alloys shows resemblance with the PdNiP BMGs that present a model case of metallic glass formation due to their high kinetic stability and large GFA at comparably simple chemical constitution, allowing for in-depth analyses of the structure and properties of a metallic glass without detrimental interference of premature crystallization or phase decompositioning. Despite similar atomic radii of sulfur and phosphorous, the compositions with the respective best glass forming ability are located at different stoichiometries with $Pd_{40}Ni_{40}P_{20}$ and $Pd_{31}Ni_{42}S_{27}$ [4,5]. Recent studies, utilizing Differential Scanning Calorimetry (DSC), revealed differences between these two sample systems with respect to their reduced glass transition temperatures $T_{rg} = T_g / T_l$, with the glass transition temperature, T_g and the liquidus temperature of the alloy composition, T_l. The difference in T_{rg} indicates that the GFA of the S-containing alloys is considerably lower, which has been confirmed experimentally. In fact, the best glass forming composition of PdNiP reaches values for T_{rg} of 0.66, with T_g = 578 K and a critical diameter of d_{cr} = 10 mm whereas T_{rg} for the best glass forming composition of PdNiS was observed at 0.58 with T_g = 430 K and d_{cr} = 1.5 mm [4]. Apart from the observed differences concerning GFA and kinetic stability between P-containing and S-containing Pd-Ni-based BMGs, the known differences of the two alloy constituents, P or S, concerning their dominant binding characteristics allow analyzing the correlations between electronic bonding characteristics such as covalency and the local atomic structure as well as the local dynamics.

Thus, the present study is focused on the comparison between the two best glass forming compositions within the systems PdNiS and PdNiP with respect to their local structure, i.e the medium-range order (MRO), and their local dynamics. MRO characterizes pair-pair correlations and thus describes structural correlations exceeding the so-called short range order that describes local motifs that are confined to the first 1–2 coordination shells. Diffraction-based analyses of the MRO correlation lengths were reported to be in the range of 1–4 nm, and even MRO size scales reaching up to 6 nm were reported [6–9]. In the present work, the MRO was analyzed in a transmission electron microscope (TEM) using Fluctuation Electron Microscopy (FEM) [10]. Relaxation dynamics in metallic glasses have often been investigated by X-ray photon correlation spectroscopy (XPCS) or DSC. These measurements provide data on the volume-averaged relaxation dynamics

* Corresponding author.
E-mail addresses: hvoigt@uni-muenster.de (H. Voigt), nico.neuber@uni-saarland.de (N. Neuber), ovaerst@uni-muenster.de (O. Vaerst), m_demm01@uni-muenster.de (M. Demming), r.busch@mx.uni-saarland.de (R. Busch), martin.peterlechner@kit.edu (M. Peterlechner), rosner@uni-muenster.de (H. Rösner), gwilde@uni-muenster.de (G. Wilde).

https://doi.org/10.1016/j.actamat.2023.119574
Received 7 February 2023; Received in revised form 13 October 2023; Accepted 3 December 2023
Available online 8 December 2023

of volumes exceeding the typical MRO length scale by many orders of magnitude. In this work, information on local dynamics with high spatial resolution was obtained using Electron Correlation Microscopy (ECM) [11]. The approach followed here offers the opportunity to analyze structure and dynamics on the length scale of the MRO. Moreover, and with respect to the observed differences of the (macroscopic) GFA of the two alloys, the TEM-based methods applied here analyze the atomic structure and its dynamics on the same length sale that also controls nucleation of crystalline phases in metallic glasses. Therefore, the current analysis also discusses possible correlations between differences in MRO and local glassy dynamics, related to different bonding characteristics, and differences in the macroscopic glass forming ability of the two Pd-Ni-based bulk glass forming alloys.

2. Methods

2.1. Sample preparation

Both glassy alloys were synthesized in bulk form. The $Pd_{31}Ni_{42}S_{27}$ samples were prepared by suction casting. High purity elements were melted in silica tubes under high purity argon atmosphere. Subsequently, the samples were fluxed through remelting in dehydrated B_2O_3 flux. Finally, the samples were suction-cast into water cooled copper molds under high purity argon atmosphere.

The $Pd_{40}Ni_{40}P_{20}$ samples were prepared from high purity ingots which were melted and cast into copper molds inside a customized melt spinner under high purity argon atmosphere.

The amorphous state of both the sulfur- and phosphorous containing samples was confirmed by X-ray diffraction and TEM measurements.

2.2. TEM measurements

TEM samples were prepared in a ZEISS Crossbeam 340 using ion beam energies of 35 keV; final polishing was done using low energy ions of 5 keV. Prior to TEM measurements, all samples were plasma cleaned for 90 s in a Fioschione Plasma Cleaner in order to avoid contamination. All TEM measurements were performed at 300 kV in an FEI Thermo Fisher Scientific Themis 300 G3 TEM. The relative thicknesses of the TEM lamellae were determined via the log ratio method using the low-loss part of the electron energy loss spectrum [12]. The reference areas for both FEM and ECM showed no thickness gradient. Also, the HAADF signal acquired in parallel during FEM measurements did not show any gradient in counts, confirming the uniform thickness [13]. Energy-dispersive X-ray (EDX) spectroscopy accompanied by high angle annular dark field scanning transmission electron microscopy (HAADF-STEM) was measured in a quadrupole energy dispersive X-ray system (Super-EDX detector) and showed no measurable compositional inhomogeneities in the regions of interest used for FEM and ECM.

2.3. Fluctuation electron microscopy

Fluctuation electron microscopy is an electron diffraction technique that gains information from the spatial fluctuations in the diffracted intensity $V(\vec{k}, R)$ of nano-sized volumes extracted from nanobeam diffraction patterns (NBDP) [8]. This can be achieved using microdiffraction operating the TEM in the scanning mode (STEM). Parallel coherent nanometer-sized probes are scanned over a sample region and the diffracted intensity variance V as a function of the scattering angle yields information on higher order structural correlations [14,15]. The normalized variance $V(\vec{k}, R)$ is a function of the scattering vector $\vec{k}$ and the spatial resolution R: $V(\vec{k}, R) = \frac{\left\langle I^2(\vec{k},R,\vec{r})\right\rangle}{\left\langle I(\vec{k},R,\vec{r})\right\rangle^2} - 1$, with $\langle\,\rangle$ being the average over sample position $\vec{r}$. The spatial resolution R is determined as the full width at half maximum (FWHM) of the electron beam, which was directly imaged on a CMOS camera (Ceta) and analyzed using a GMS™ (Gatan) script from Dave Mitchell [16]. Systematically varying the probe size is called variable resolution FEM (VR-FEM). This method allows for the measurement of the MRO length scale, MRO volume fraction or anisotropy/strain [17]. The experimental normalized variance profiles were calculated using the annular mean of variance image [18]. For the VR-FEM data evaluation, the maximum normalized variance and its position were determined using a Gaussian fit in the k range between 4 and 5.5 1/nm. For each normalized variance curve, $V_{max}(R)$ was plotted against $1/R^2$ according to the Stratton–Voyles model [19]. When the probe size coincides with the scattering MRO length scale a peak or plateau occurs in these curves. For the estimation of the MRO volume fraction, the normalized variance curves peak heights have been used, which are a semi-quantitative measure [7,9,17].

NBDP series were acquired using a beam current of 15 pA and probe sizes between 0.8 and 6.6 nm at FWHM. The acquisition time for the individual NBDPs was set to 4 s and a binning of 4 was used to ensure a high signal-to-noise ratio. It was made sure that all parameters influencing the diffraction intensity such as foil-thickness, exposure time and beam current were kept constant for all samples to allow for a detailed and unambiguous comparison between the two alloy systems.

2.4. Electron correlation microscopy

Electron Correlation Microscopy uses intensity changes of tilted dark-field (t-DF) micrographs to extract local dynamics [11]. Dynamics in (metallic) glasses can often be described by a Kohlrausch–Williams–Watts (KWW)-function $g_2(t) = 1 + A \cdot \exp(-(\frac{t}{\tau})^{\beta})$ [20,21], where β is the stretching exponent, τ the average relaxation time and A an instrument dependent scaling parameter. From a t-DF micrograph series, a time correlation can be calculated using the autocorrelation function: $g_2(t) = \frac{\left\langle I(t')I(t'+t)\right\rangle}{\left\langle I(t')\right\rangle^2}$. Pixelwise fitting of a KWW-function to the acquired time correlation yields a map of relaxation dynamics in the form of τ- and β-maps. Thus, the ECM results give a metric for the speckle lifetime per pixel and position and consequentially for the structural dynamics of the glass at the specific experimental parameters such as temperature, time and electron dose.

Prior to the fitting of the KWW-function, a logarithmic resampling of the data was performed to avoid an increase in the data point density for longer exposure times. Moreover, a certain fraction of the data points in the PdNiS τ-maps was set to zero in case that the calculated autocorrelations were deviating more than 15 % from the mean. A total of 5421 pixels were set to 0, which is the equivalent of about 1.2% of all pixels analyzed. Thus, crystallization events, even if they would occur, were excluded from the analysis. Excluding the pixels set to zero artificially lowers the calculated averaged τ-times. However, since the fraction of pixels is low, the overall estimation of relaxation times is still valid.

Each data set was acquired over a period of 18150 s and contained 3630 individual t-DF images, each frame had a dwelltime of 4 s with a wait time of 1 s in between frames. For comparability, all ECM measurements were performed under identical experimental conditions, including the electron dose which was kept constant at $1.5 \cdot 10^5$ $e^-/(nm^2\ s)$. It is worth noting that it is essential to keep the parameters constant to ensure a similar sample-beam interaction, because it has been shown that there is an artificial electron beam induced speed-up of relaxation dynamics [22].

The standard ECM approach assumes a steady state, termed quasi-thermodynamic equilibrium [23], which describes the requirement that the investigated system needs to be stationary with respect to irreversible long-range rearrangements on the time scale of the measurement, to achieve a robust metric for the local dynamics [11].

3. Results and discussion

3.1. Fluctuation electron microscopy

Normalized variance curves for both investigated sample systems, i.e. $Pd_{40}Ni_{40}P_{20}$ and $Pd_{31}Ni_{42}S_{27}$, are shown in Fig. 1. Two peaks are observed for both sample systems with the first peak being the more prominent one. The first peak in the normalized variance curves is located at $k_{1stpeak}^{sulfur}$ = 4.64 ± 0.02 1/nm for the $Pd_{31}Ni_{42}S_{27}$ glass whereas the first peak appears at $k_{1stpeak}^{phosphorous}$ = 4.74 ± 0.02 1/nm for $Pd_{40}Ni_{40}P_{20}$. This difference of the k-values amounts to about 2 % and can be attributed to differences in the prevalent MRO correlation length. Structurally, the differences of the correlation length of the MRO might be related to an increase of the excess free volume in the sulfur-containing alloy [24] or to a difference in packing density. Both alternative interpretations would be in line with topological expectations for a more covalently bonding system due to the larger steric hindrances involved when the directionality of interatomic bonds is increased.

When plotting the probe size-dependent peak heights $V_{1stpeak}$ as Stratton–Voyles plots (see Fig. 2), two aspects are directly observable for both systems. First, the maximum variance is reached for similar probe sizes, i.e. 1.6 ± 0.5 in the sulfur-containing and 1.7 ± 0.5 nm in the phosphorous-containing system, implying that the underlying correlation lengths are similar. Second, a significant difference of the absolute values of the normalized variance for the smallest correlation lengths was observed, which occur at $V_{1stpeak}^{sulfur}$ = 0.142 and at $V_{1stpeak}^{phosphorous}$ = 0.196. The peak height in a Stratton–Voyles-plot is a semi-quantitative measure for the MRO volume fraction. Here, only the peak height of the most prominent correlation length present in both systems was used for comparison, revealing a relative decrease of the MRO volume fraction for the $Pd_{31}Ni_{42}S_{27}$ as compared to the $Pd_{40}Ni_{40}P_{20}$ glass.

Highly stable glasses can be characterized as having both a low Gibbs free energy and a large activation energy for crystallization. The observed difference of the MRO volume fractions of the two Pd–Ni-based BMGs might be related to their respective thermal stabilities, i.e. the values of T_{rg} of the two glasses. A direct correlation between the underlying motifs of MRO and the observed changes in the MRO was not possible here, but might be possible by applying reverse Monte Carlo simulations. It has been shown that MRO observed in metallic glasses can have both icosahedral and crystalline motifs, while there are reports of almost perfect icosahedral configurations present in the $Pd_{40}Ni_{40}P_{20}$ glass [25,26]. Thus, under the assumption that the prevailing MRO present in both glasses is of icosahedral nature it could be speculated that with increasing local microscopic or mesoscopic structural order, the Gibbs free energy is reduced. Consequently, an increase of the MRO volume fraction would increase the thermodynamic stability of the glass. This assumption can be substantiated by thermodynamic calculations on the basis that the driving force for the nucleation process in glasses can be estimated through the difference in Gibbs free energy between the liquid and the primary crystalline phase ΔG^{l-x}, i.e. the thermodynamic "driving force" for nucleation. Applying Turnbull's approximation [4,27], ΔG^{l-x} can be approximated by the entropy of fusion. The respective entropies of fusion for $Pd_{40}Ni_{40}P_{20}$ and $Pd_{31}Ni_{42}S_{27}$ have been determined in earlier DSC studies as 8.6 J g-atom^{-1} K^{-1} and 14.2 J g-atom^{-1} K^{-1}, respectively, revealing a higher thermodynamic tendency to form crystals for $Pd_{31}Ni_{42}S_{27}$ [4,28]. A combination of both, the structural and thermodynamic arguments, leads to a qualitative explanation for the strong difference in T_{rg} and GFA of $Pd_{40}Ni_{40}P_{20}$ and $Pd_{31}Ni_{42}S_{27}$.

Up to this point, no unambiguous assessment can be made whether the addition of sulfur promotes the formation of covalent bonds, although suggestions have been made that sulfur can enhance the formation of covalent bonds in the glass forming alloy TiNiS [29]. Previously, theoretical studies suggested that in the $Pd_{40}Ni_{40}P_{20}$ glass, $(Ni,Pd)_9P$

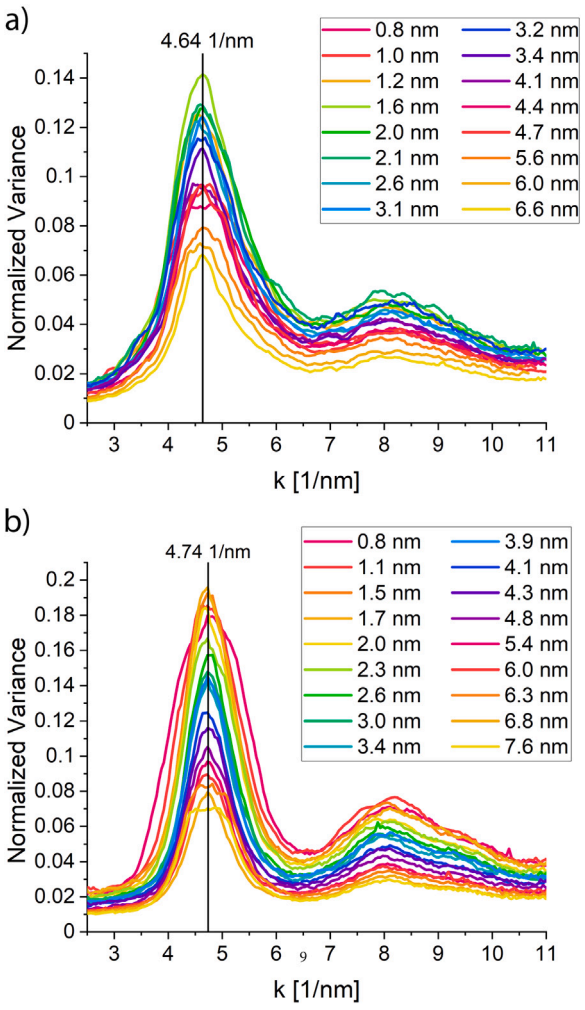

Fig. 1. Normalized variance curves of (a) $Pd_{31}Ni_{42}S_{27}$ and (b) $Pd_{40}Ni_{40}P_{20}$ acquired with different probe sizes. The first peak maxima are observed at 4.64 nm^{-1} and 4.74 nm^{-1}, as indicated by the black lines. Data for $Pd_{40}Ni_{40}P_{20}$ was taken from [9]. (For interpretation of the references to color in this figure legend, the reader is referred to the web version of this article.)

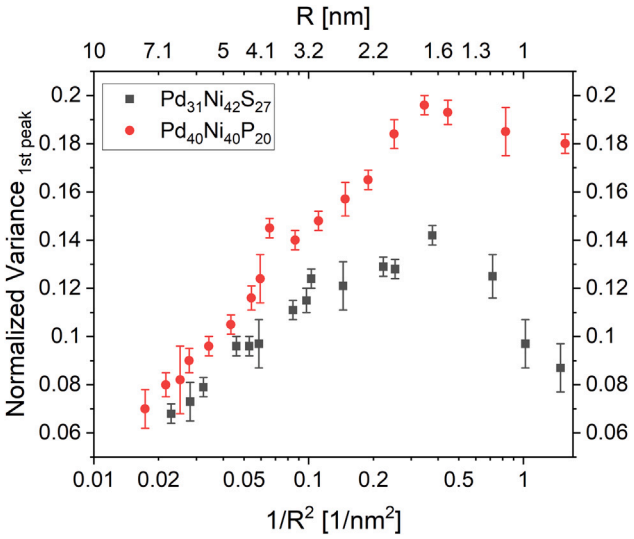

Fig. 2. FEM analysis visualized in the form of Stratton–Voyles plots, i.e. peak height at the first maximum in the normalized variance curves plotted against $1/R^2$, are shown for $Pd_{31}Ni_{42}S_{27}$ and $Pd_{40}Ni_{40}P_{20}$.

Table 1
Parameters of the KWW-function fitted perpendicular to the main diagonal of the TTCF. For the fitting over 5000 s were averaged and centered around different waiting times.

Sample	Center [s]	τ [s]	β	R^2
$Pd_{31}Ni_{42}S_{27}$	6150	449 ± 6	0.55 ± 0.01	0.93
	11 400	528 ± 7	0.46 ± 0.01	0.91
$Pd_{40}Ni_{40}P_{20}$	6150	2727 ± 4	0.59 ± 0.01	0.99
	11 400	2354 ± 4	0.63 ± 0.01	0.98

Table 2
Parameters of the KWW-function fitted to the (g_2-1)/A functions calculated from the tilted DF-time series.

Sample	τ [s]	β
$Pd_{40}Ni_{40}P_{20}$	1928 ± 4	0.76 ± 0.01

trigonal prism clusters with a phosphorous atom in the center and a covalent nature could be present [30]. Similar behavior could be expected for the sulfur-containing glasses due to the fact that the atomic radii of sulfur and phosphorous are comparable and the electronegativity of sulfur EN_{sulfur} = 2.58 after Pauling is even larger than that of phosphorous $EN_{phosphorous}$ = 2.19. Thus, a more directional bonding character can be assumed for the S-containing alloys, further promoting the hypothesis that covalent bonding might be more significant in the Sulfur-containing glasses. However, the differences in electron configuration and electronegativity between phosphorus and sulfur do not seem to have an impact on the MRO length scale, which is rather surprising since a hybridization of sulfur could be expected, which would result in smaller bond lengths and more directional bonds.

Moreover, as indicated by an analysis performed by Scopigno et al. and Schnabel et al. [31,32], a larger directionality of bonds (i.e. stronger covalent contributions to the total binding energy) should lead to more stable glasses. While this tendency is understandable in terms of steric reasons, it should also be considered that these analyses were performed for different systems, i.e. non-metallic glasses or thin-film metallic glasses of low GFA.

3.2. Electron correlation microscopy

Two-time correlation functions (TTCF) were calculated for both $Pd_{40}Ni_{40}P_{20}$ and $Pd_{31}Ni_{42}S_{27}$ from a 540 × 430 pixel area, providing good statistics and are shown in Fig. 3. From visual inspection for both sample systems, no narrowing or broadening of the main diagonal was observed, indicating neither beam-driven acceleration of dynamics nor aging within the temporal observation window. For a more quantitative evaluation selective relaxation times averaged over more than 5000 s centered around waiting times of 6150 s and 11400 s were calculated by investigating the decorrelations perpendicular to the main diagonal of the TTCF (see Fig. 4) [23,33]. Such averaging was required to ensure a good signal-to-noise ratio. At both waiting times the decorrelations were fitted using a KWW-function as shown in Fig. 4. The deviation in relaxation times between waiting times was calculated to be of the order of 15 % for both sample systems, and the corresponding fitting parameters are listed in Table 1. We can thus assume that these kind of deviations of the order of 15 % are method based since it is found to be similar for both samples. However, it is obvious that the relaxation times in the sulfur based system are smaller than in the phosphorus based one; this will be focused on in more detail in the next section. Thus, it can be concluded that neither of the systems experienced stronger narrowing or broadening of the main diagonal.

3.2.1. Composition-induced differences of the local dynamics

Quantification of the relaxation dynamics was done via averaging the auto-correlation over all positions of the sample. The spatially averaged (g_2-1)/A functions for both systems are shown in Fig. 5(a) and 5(b) together with single KWW-fits, respectively fitted to them. It

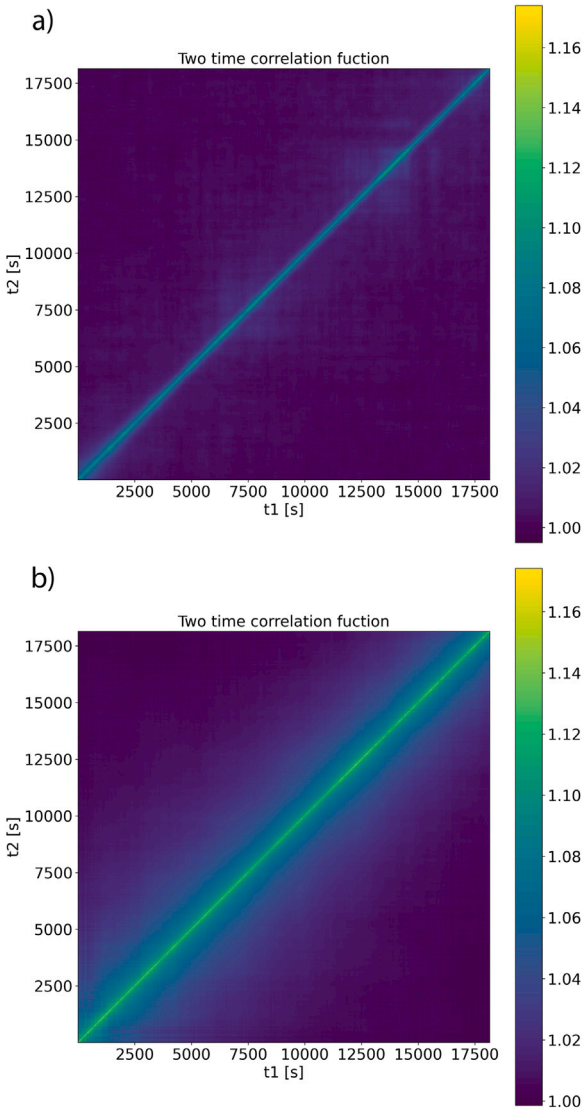

Fig. 3. Two-time correlation functions calculated for (a) $Pd_{31}Ni_{42}S_{27}$ and (b) $Pd_{40}Ni_{40}P_{20}$. No narrowing or broadening could be observed, ensuring quasi-thermodynamic equilibrium.

is important to note that, given the (4 + 1) s exposure time for each frame, there are only two data points between 10^0 and 10^1 s. This might be confusing because the time axis is logarithmically scaled. The corresponding fitting parameters are listed in Table 2 and confirm that the local dynamics at room temperature are considerably faster in the sulfur-containing glass.

The different local dynamics have to be discussed, considering the different glass transition temperatures. In fact, both materials have a different ratio of T/T_g at room temperature, which in the following is referred to as homologous glass transition temperature T_{HG}. They are calculated to be $T_{HG}^{sulfur} = 0.69$ and $T_{HG}^{phosphorous} = 0.51$. Since $Pd_{31}Ni_{42}S_{27}$ at room temperature is closer to T_G, it is expected to show faster dynamics and, as a consequence, to be less stable.

3.2.2. Heterogeneity of local dynamics in Pd_{31} $Ni_{42}S_{27}$

In Figs. 5(c) and 5(d) the spatially resolved dynamics of both systems are displayed in the form of τ-maps. From these τ-maps it is apparent that rather well-defined, distinct regions with relatively slower dynamics exist in the $Pd_{31}Ni_{42}S_{27}$ system, whereas this heterogeneity does not exist in the $Pd_{40}Ni_{40}P_{20}$ system. These regions

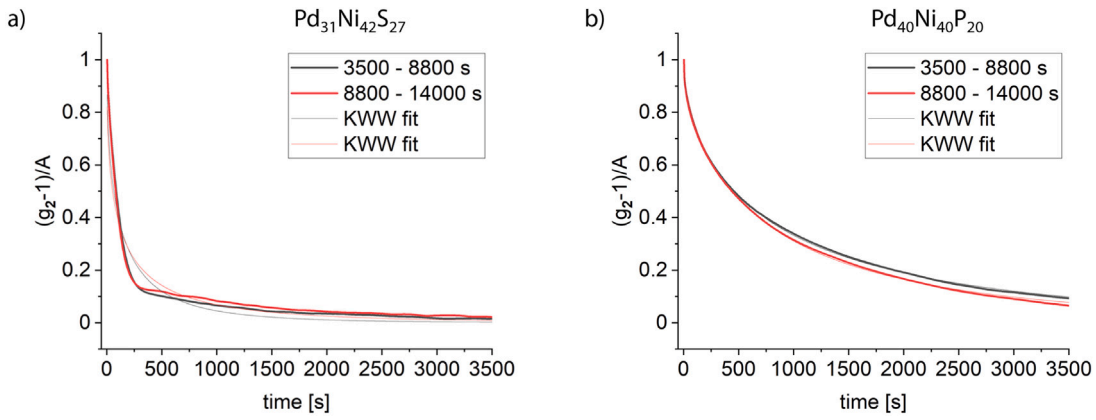

Fig. 4. Comparison of the momentary relaxation times calculated at different waiting times for (a) $Pd_{31}Ni_{42}S_{27}$ and (b) $Pd_{40}Ni_{40}P_{20}$.

have not yet crystallized as shown by the TTCF and have an average diameter of about 5–8 nm, i.e. their size is considerably larger than the characteristic size scale of the MRO. While these regions might appear as indicative of mesoscopically coherent dynamics, it should be noted that any spatio-temporal coherence cannot be analyzed by the present approach. The local regions observed in Fig. 5(c) indicate the existence of regions where rearrangement during the duration of the measurement occurred at comparable dynamics. This in itself is an interesting observation, hinting to a length scale for dynamic heterogeneity. Yet, whether those rearrangements occurred cooperatively or not can unfortunately not be assessed on the basis of the present analysis and represents a topic for further method development and investigation.

The τ-distributions for both systems are shown in Figs. 5(e) and 5(f). It is possible to describe the distribution in $Pd_{40}Ni_{40}P_{20}$ as lognormal. In contrast, the data obtained on $Pd_{31}Ni_{42}S_{27}$ can be described with reasonably high accuracy using the superposition of two lognormal distributions, while the fit with only one lognormal distribution renders a considerably larger error to the best fit. The superposition of two lognormal distribution functions can be interpreted as the existence of two types of regions with different mean relaxation times, where the partial distribution at higher characteristic times for rearrangement has a lower volume percentage. Thus, it is assumed that this distribution is correlated to the distinct regions of slower dynamics in the $Pd_{31}Ni_{42}S_{27}$ BMG.

In a molecular dynamics (MD) simulation the impact of structural and dynamic heterogeneity on the crystallization was investigated. One of their principal conclusions was that structural pre-ordering involving a decrease in mobility promotes nucleation [34]. Similar results have been obtained from unsupervised machine learning studies [35]. Consequently, the assumption can be made that the clustered regions with slower dynamics might act as precursors for crystallization. It should be stressed that the regions of slower dynamics are interpreted as regions where the slow-down of dynamics might indicate a larger fertility of these regions to form a crystalline phase at either longer times or higher temperatures. This hypothesis is in line with the observed tendency of $Pd_{31}Ni_{42}S_{27}$ to crystallize more readily, i.e. to present lower kinetic stability and lower GFA as compared to the $Pd_{40}Ni_{40}P_{20}$ BMG.

4. Summary and conclusions

The results of the present study demonstrate the impact of sulfur on the MRO in a bulk metallic glass by comparing the most stable configurations of ternary PdNi-based metalloid BMG with phosphorous or sulfur as the third alloying elements. The absolute MRO correlation length appears not to be affected by varying the metalloid from phosphorous to sulfur and is of the order of 1.6–1.7 nm. However, the MRO volume fraction is observed to be significantly different for the two alloy systems. The relative reduction of the MRO volume fraction of the sulfur-containing glass might be related to the lower kinetic stability of $Pd_{31}Ni_{42}S_{27}$ as compared to $Pd_{40}Ni_{40}P_{20}$. In this line of argument, a topologically more ordered system, e.g. given by an increased icosahedral-like MRO volume fraction, should have a reduced Gibbs free energy compared to a less ordered system. This reduction of Gibbs free energy could be the reason for the lower thermal stability of the $Pd_{31}Ni_{42}S_{27}$ BMG as compared to the phosphorous-containing glass.

The difference in the first peak position of the normalized variance curves can either be interpreted as a change in excess free volume or a change in packing density. For the packing density Φ calculation, a simple estimation based on hard spheres was made as follows: $\Phi = \bar{V}\rho N_a/\bar{M}$, where ρ is the density, N_a the Avogadro constant, $\bar{M}$ the average molar mass and $\bar{V}$ the weighted mean atomic volume of the 'average' hard spheres. The respective packing densities were determined to be $\Phi^S = 0.40$ for $Pd_{31}Ni_{42}S_{27}$ and $\Phi^P = 0.61$ for $Pd_{40}Ni_{40}P_{20}$. These calculated values are representing the same trend observable from the NBDP analysis while there is an expected discrepancy in the absolute values.

The presence of sulfur also does seem to have an impact on the local dynamics of atomic rearrangements in the glass at room temperature. In the $Pd_{31}Ni_{42}S_{27}$ glass overall faster dynamics were observed as compared to the $Pd_{40}Ni_{40}P_{20}$ glass, which is in agreement with the relative magnitudes of the homologous glass transition temperatures of $T_{HG}^{sulfur} = 0.69$ and $T_{HG}^{phosphorous} = 0.51$. Interestingly, distinct regions with slower dynamics have been observed for the $Pd_{31}Ni_{42}S_{27}$ BMG, which might act as precursors for nucleation, in agreement with previous studies determining that $Pd_{31}Ni_{42}S_{27}$ is more likely to crystallize.

Nonetheless, the underlying mechanism of the relation between the detected regions of slower dynamics and the onset of crystallization needs to be examined more thoroughly in experiments to come. At this point we suggest three hypotheses that require concerted experiments and theoretical studies to distinguish between the alternatives:

- The onset of crystallization is the immediate effect caused by a cooperatively re-arranging region with altered relaxation dynamics. This theory is closely following the concept of Adam and Gibbs [36].
- The dynamics are changed due to a local rearrangement of atoms. Regions exhibiting increased order or crystal-like motifs slow down the dynamics.
- The onset of nucleation itself causes the change in relaxation dynamics.

This study thus highlights the drastic changes in structure and relaxation dynamics that are introduced when exchanging alloying elements, such as phosphorous with sulfur.

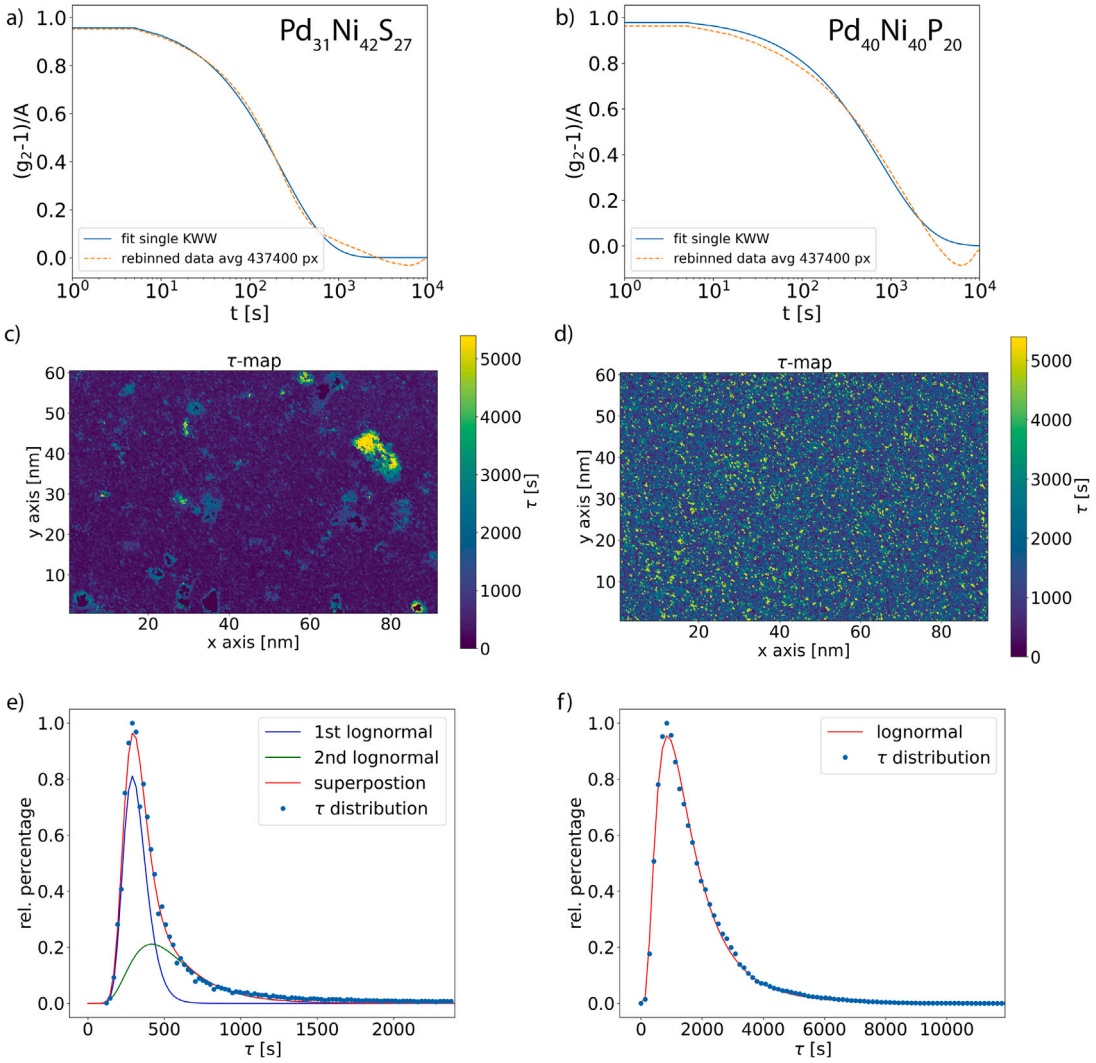

Fig. 5. ECM analysis of $Pd_{31}Ni_{42}S_{27}$ and $Pd_{40}Ni_{40}P_{20}$. (a) and (b) show fits of a single KWW to the normalized autocorrelation function averaged over 437400 pixel. Spatially resolved relaxation times are shown in (c) and (d) as τ-maps displaying the fitting parameter at each pixel. τ-Distributions with lognormal fits are displayed in (e) and (f). (Left: $Pd_{31}Ni_{42}S_{27}$, Right: $Pd_{40}Ni_{40}P_{20}$).

Last but not least, the present study could correlate, for the first time, the relaxation dynamics at temperatures below the glass transition in metallic glasses with structural modifications on the nanometer scale. These results indicate a route for addressing long-standing issues concerning the possible structural origins of glassy dynamics and dynamic heterogeneity of glassy systems.

Declaration of competing interest

The authors declare that they have no known competing financial interests or personal relationships that could have appeared to influence the work reported in this paper.

Acknowledgments

Financial support from the German Science Foundation (DFG) via research grants Wi 1899/38-1 and BU 2276/11-1 is acknowledged. The DFG is further acknowledged for funding our TEM equipment via the Major Research Instrumentation Program under INST 211/719-1 FUGG. The authors would like to thank Dražen Radić for FIB preparation.

References

[1] W. Klement, R.H. Willens, P. Duwez, Non-crystalline structure in solidified gold–silicon alloys, Nature 187 (4740) (1960) 869–870.
[2] D. Turnbull, The undercooling of liquids, Sci. Am. 212 (1) (1965) 38–47.
[3] A. Kuball, O. Gross, B. Bochtler, R. Busch, Sulfur-bearing metallic glasses: A new family of bulk glass-forming alloys, Scr. Mater. 146 (2018) 73–76.
[4] A. Kuball, B. Bochtler, O. Gross, V. Pacheco, M. Stolpe, S. Hechler, R. Busch, On the bulk glass formation in the ternary Pd-Ni-S system, Acta Mater. 158 (2018) 13–22.
[5] Y. He, R.B. Schwarz, J.I. Archuleta, Bulk glass formation in the Pd-Ni-P system, Appl. Phys. Lett. 69 (13) (1996) 1861–1863.
[6] R.K. Dash, P.M. Voyles, J.M. Gibson, M.M.J. Treacy, P Keblinski, A quantitative measure of medium-range order in amorphous materials from transmission electron micrographs, J. Phys.: Condens. Matter 15 (31) (2003) S2425.
[7] S.N. Bogle, L.N. Nittala, R.D. Twesten, P.M. Voyles, J.R. Abelson, Size analysis of nanoscale order in amorphous materials by variable-resolution fluctuation electron microscopy, Ultramicroscopy 110 (10) (2010) 1273–1278.
[8] P.M. Voyles, D.A. Muller, Fluctuation microscopy in the STEM, Ultramicroscopy 93 (2) (2002) 147–159.
[9] S. Hilke, H. Rösner, G. Wilde, The role of minor alloying in the plasticity of bulk metallic glasses, Scr. Mater. 188 (2020) 50–53.
[10] M.M.J. Treacy, J.M. Gibson, L. Fan, D.J. Paterson, I. McNulty, Fluctuation microscopy: A probe of medium range order, Rep. Progr. Phys. 68 (12) (2005) 2899.
[11] L. He, P. Zhang, M. F Besser, M.J. Kramer, P.M. Voyles, Electron correlation microscopy: A new technique for studying local atom dynamics applied to a supercooled liquid, Microsc. Microanal. 21 (4) (2015) 1026–1033.

[12] T. Malis, S.C. Cheng, R.F. Egerton, EELS log-ratio technique for specimen-thickness measurement in the TEM, J. Electron Microsc. Technique 8 (2) (1988) 193–200.
[13] F. Yi, P.M. Voyles, Effect of sample thickness, energy filtering, and probe coherence on fluctuation electron microscopy experiments, Ultramicroscopy 111 (8) (2011) 1375–1380.
[14] M.M.J. Treacy, J.M. Gibson, Variable coherence microscopy: A rich source of structural information from disordered materials, Acta Crystallogr. A: Found. Crystallogr. 52 (2) (1996) 212–220.
[15] P.M. Voyles, J.M. Gibson, M.M.J. Treacy, Fluctuation microscopy: A probe of atomic correlations in disordered materials, Microscopy 49 (2) (2000) 259–266.
[16] D.R.G. Mitchell, B. Schaffer, Scripting-customised microscopy tools for digital micrograph™, Ultramicroscopy 103 (4) (2005) 319–332.
[17] S.N. Bogle, P.M. Voyles, S.V. Khare, J.R. Abelson, Quantifying nanoscale order in amorphous materials: Simulating fluctuation electron microscopy of amorphous silicon, J. Phys.: Condens. Matter 19 (45) (2007) 455204.
[18] T.L. Daulton, K.S. Bondi, K.F. Kelton, Nanobeam diffraction fluctuation electron microscopy technique for structural characterization of disordered materials-Application to Al88-x Y7Fe5Tix metallic glasses, Ultramicroscopy 110 (10) (2010) 1279–1289.
[19] W.G. Stratton, P.M. Voyles, A phenomenological model of fluctuation electron microscopy for a nanocrystal/amorphous composite, Ultramicroscopy 108 (8) (2008) 727–736.
[20] P. Zhang, J.J. Maldonis, Z. Liu, J. Schroers, P.M. Voyles, Spatially heterogeneous dynamics in a metallic glass forming liquid imaged by electron correlation microscopy, Nat. Commun. 9 (1) (2018) 1–7.
[21] S.H. Chung, J.R. Stevens, Time-dependent correlation and the evaluation of the stretched exponential or Kohlrausch-Williams-Watts function, Amer. J. Phys. 59 (11) (1991) 1024–1030.
[22] K. Spangenberg, S. Hilke, G. Wilde, M. Peterlechner, Direct view on non-equilibrium heterogeneous dynamics in glassy nanorods, Adv. Funct. Mater. 31 (38) (2021) 2103742.
[23] A. Das, E.M. Dufresne, R. Maaß, Structural dynamics and rejuvenation during cryogenic cycling in a Zr-based metallic glass, Acta Mater. 196 (2020) 723–732.
[24] Y.F. Deng, L.L. He, Q.S. Zhang, H.F. Zhang, H.Q. Ye, HRTEM analysis of nanocrystallization during uniaxial compression of a bulk metallic glass at room temperature, Ultramicroscopy 98 (2–4) (2004) 201–208.
[25] C. Gammer, B. Escher, C. Ebner, A.M. Minor, H. Karnthaler, J. Eckert, S. Pauly, C. Rentenberger, Influence of the Ag concentration on the medium-range order in a CuZrAlAg bulk metallic glass, Sci. Rep. 7 (1) (2017) 44903.
[26] S. Hosokawa, J. Bérar, N. Boudet, W. Pilgrim, L. Pusztai, S. Hiroi, K. Maruyama, S. Kohara, H. Kato, H.E. Fischer, et al., Partial structure investigation of the traditional bulk metallic glass Pd40Ni40P20, Phys. Rev. B 100 (5) (2019) 054204.
[27] D. Turnbull, Under what conditions can a glass be formed? Contemp. Phys. 10 (5) (1969) 473–488.
[28] G. Wilde, G.P. Görler, R. Willnecker, G. Dietz, Thermodynamic properties of Pd40Ni40P20 in the glassy, liquid, and crystalline states, Appl. Phys. Lett. 65 (4) (1994) 397–399.
[29] J. Wilden, F. Yang, D. Holland-Moritz, S. Szabó, W. Lohstroh, B. Bochtler, R. Busch, A. Meyer, Impact of sulfur on the melt dynamics of glass forming Ti75Ni25-xSx, Appl. Phys. Lett. 117 (1) (2020) 013702.
[30] T. Takeuchi, D. Fukamaki, H. Miyazaki, K. Soda, M. Hasegawa, H. Sato, U. Mizutani, T. Ito, S. Kimura, Electronic structure and stability of the PdNiP bulk metallic glass, Mater. Trans. 48 (6) (2007) 1292–1298.
[31] T. Scopigno, G. Ruocco, F. Sette, G. Monaco, Is the fragility of a liquid embedded in the properties of its glass? Science 302 (5646) (2003) 849–852.
[32] V. Schnabel, B.N. Jaya, M. Köhler, D. Music, C. Kirchlechner, G. Dehm, D. Raabe, J.M. Schneider, Electronic hybridisation implications for the damage-tolerance of thin film metallic glasses, Sci. Rep. 6 (1) (2016) 1–12.
[33] A. Das, P.M. Derlet, C. Liu, E.M. Dufresne, R. Maaß, Stress breaks universal aging behavior in a metallic glass, Nat. Commun. 10 (1) (2019) 5006.
[34] G.D. Leines, A. Michaelides, J. Rogal, Interplay of structural and dynamical heterogeneity in the nucleation mechanism in nickel, Faraday Discuss. (2022).
[35] C.S. Adorf, T.C. Moore, Y.J.U. Melle, S.C. Glotzer, Analysis of self-assembly pathways with unsupervised machine learning algorithms, J. Phys. Chem. B 124 (1) (2019) 69–78.
[36] G. Adam, J.H. Gibbs, On the temperature dependence of cooperative relaxation properties in glass-forming liquids, J. Chem. Phys. 43 (1) (1965) 139–146.